Tunability of Subradiant Dipolar and Fano-Type Plasmon Resonances in Metallic Ring/Disk Cavities: Implications for Nanoscale Optical Sensing

Feng Hao,[†] Peter Nordlander,[†,*] Yannick Sonnefraud,[‡] Pol Van Dorpe,[§] and Stefan A. Maier[‡,*]

[†]Laboratory for Nanophotonics, Department of Physics and Astronomy, M.S. 61, Rice University, Houston, Texas 77005-1892, [‡]Experimental Solid State Group, Physics Department, Imperial College, London SW7 2AZ, United Kingdom, and [§]IMEC, Kapeldreef 75, 3001 Leuven, Belgium

ABSTRACT Plasmonic nanocavities consisting of the concentric arrangement of a disk and a ring sustain both subradiant and superradiant dipolar plasmon modes with large associated field enhancements and high refractive index sensitivities. In structures with broken symmetry, additionally a highly tunable Fano interference feature appears, which can be explained with a simple analytical harmonic oscillator model. The spectral tunability of these resonances from the visible to the mid-infrared is investigated, highlighting a potential for applications in surface enhanced spectroscopies.

KEYWORDS: plasmonics · optical nanocavities · surface enhanced spectroscopy · Fano resonances

Research on the optical properties of metallic nanostructures supporting localized surface plasmon resonances has flourished over the past decade, spurred by advances in nanofabrication, nano-optical characterization, and improvements in full-field computational electromagnetics. This has led to the emergence of the field of nanoplasmonics.[1−4] Plasmon resonances of isolated nanostructures can be tuned throughout the visible and near-infrared part of the spectrum with particles of simple geometrical shapes such as disks, triangles, rods, and rings.[5−7] This wide parameter space for the creation of optical modes with often deep subwavelength effective mode volumes[8,9] holds the promise for nanoplasmonics to develop into a disruptive technology for applications ranging from surface enhanced spectroscopies[10−12] to nanoshell-based cancer therapies.[13]

The richness of the optical response of a metallic nanostructure of a given shape depends in the first instance on its characteristic size d. In the quasi-static regime with $d \ll \lambda$, where λ is the wavelength in the surrounding dielectric, the nanostructure shows mainly a dipolar-like response. However, also higher-order resonances can be made to couple to an incident electromagnetic field if the symmetry of the structure is broken, allowing a mixing between otherwise dark multipolar modes with the bright dipolar modes.[14] This has recently been exploited in a metamaterials context.[15−18] An increase in size beyond the quasi-static limit on the other hand makes higher-order modes directly dipole-active due to retardation effects,[19,20] varying with the angle of incidence of the illuminating radiation. An even richer spectral response emerges in more complex structures consisting of multiple metallic elements separated by nanoscale dielectric gaps, which within the plasmon hybridization framework[21] can be decomposed into bonding and antibonding type combinations of the constituent fundamental plasmon resonances (dipolar and higher), leading in essence to *plasmonic molecules*.

Plasmonic nanostructures therefore act as physically realizable classical oscillator systems on the nanoscale, which apart from their application potential makes them model systems for a variety of fascinating physical processes. For example, in structures with broken symmetry, Fano resonances can appear due to the interaction of narrow dark modes with broad bright modes. This phenomenon has been theoretically investigated for a variety of structures ranging from particle lattices and split-ring-type structures to nanowire arrays and particle dimers.[15,18,22−24] For strongly coupled systems and near-degenerate levels, the asymmetric Fano line shape will evolve into a plasmonic-induced optical transparency of the nanostructure,[25] in a

*Address correspondence to nordland@rice.edu, S.Maier@imperial.ac.uk.

Received for review January 7, 2009 and accepted January 28, 2009.

Published online February 9, 2009.
10.1021/nn900012r CCC: $40.75

classical analogue[26] to the well-known phenomenon of electromagnetically induced transparency (EIT) of atomic physics.

We have recently described a plasmonic nanostructure with a particularly high tunability, the concentric ring/disk cavity (CRDC).[27] This structure sustains both subradiant and superradiant dipolar modes set up *via* hybridization of individual disk and ring plasmons. The subradiant mode exhibits a substantially narrower line width and higher field enhancement than the parent plasmons. A significant potential for surface enhanced spectroscopies both in the visible and at the same time in the near/mid-infrared was identified, due to a highly tunable spectral separation of the dipolar modes. The field enhancement is further increased when the symmetry of the structure is broken, and higher order multipolar modes become dipole-active. Such a noncentric ring/disk cavity (NCRDC) additionally exhibits a highly tunable Fano resonance in the extinction spectrum, similar to the EIT phenomenon.[28]

In this publication, we discuss the tunability of the plasmon resonance spectrum of both CRDCs and NCRDCs in detail, with a viewpoint of applications in surface enhanced spectroscopies and localized surface plasmon resonance (LSPR) refractive index sensing. To this end, we quantify the attainable field enhancements for cavities on substrates, and the refractive index sensitivities, of both dipolar and Fano-type modes in the visible, near-infrared, and mid-infrared. We further elucidate the fundamental physics of this oscillator system in a description based on plasmon hybridization.

RESULTS AND DISCUSSION

We start our discussion with the modal properties of the symmetric system, the CRDC. The geometry is defined by four parameters as in Figure 1a: the inner and outer diameters of the ring d_1 and d_2, the diameter of the inner disk D, and cavity height H. For a finite size of the gap between disk and ring, we hence have $D < d_1 < d_2$. No significant dependence of the extinction spectra on the detailed shape of the cross section was found, hence a simple perfect cylindrical shape is used throughout for the modeling. For all structures presented in our discussions, the metal of choice is Au, due to its amenability for surface functionalization with a viewpoint to molecular sensing.

We have previously shown that the extinction spectrum of a CRDC in vacuum can be well explained as the hybridization of individual disk and ring plasmons.[27] The basic concept is illustrated in the extinction spectra of Figure 1b for a structure with $d_2 = 200$ nm, $d_1 = 100$ nm, $D = 80$ nm, and $H = 50$ nm. The left and right panels show the extinction spectra of the individual structures, with the dipolar disk mode and the bonding ring mode[7] clearly visible. The intensity of the high-energy antibonding dipolar ring resonance, characterized by an antisymmetric alignment of the surface

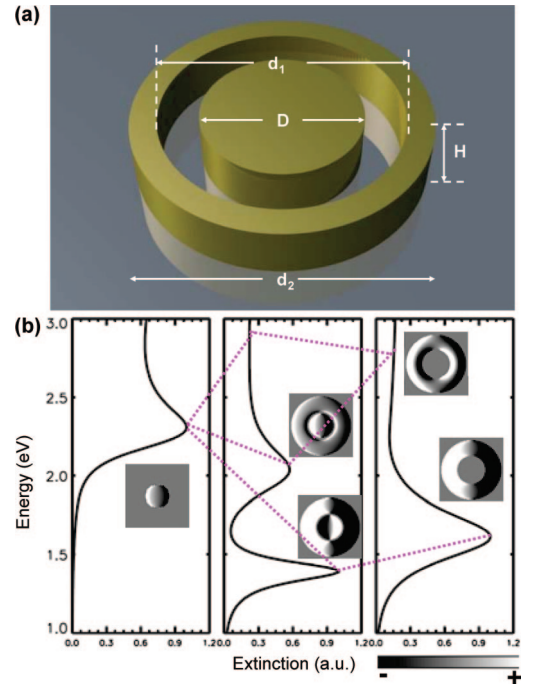

Figure 1. (a) Geometry of a concentric ring/disk cavity (outer ring diameter d_2, inner diameter d_1, disk diameter D, and height H). (b) Hybridization diagram for a Au structure in vacuum with $d_2 = 200$ nm, $d_1 = 100$ nm, $D = 80$ nm, and $H = 50$ nm obtained using FDTD simulations of the extinction cross section of the combined cavity (center panel) and the individual structures (left and right panel). The subradiant (DBR) mode below 1.5 eV for the combined structure results mainly through bonding-type hybridization of oppositely aligned (bonding) ring and disk dipoles. The superradiant (DAR) mode around 2.0 eV is mainly a bonding combination of the (antibonding) ring dipole and the primitive disk dipole.

charges on the inner and outer ring walls, is as expected very weak compared to the low-energy bonding ring resonance, due to its low coupling to the electromagnetic field and the influence of interband damping. The symmetries of the modes are clearly revealed in the pictures of the respective modal surface charge distributions, shown in the inset. The center panel shows the extinction spectrum of the combined system with two modes set up *via* hybridization of individual disk and ring dipolar plasmons, indicated with dotted lines. The broad hybridized resonance around 2.0 eV is mainly a bonding combination of the antibonding ring dipole and the disk dipole. We will refer to this mode as the DAR mode. A small component of bonding ring mode is also mixed in the DAR mode. However, the down shift in energy of the DAR mode compared to the bonding disk mode and the charge distribution clearly demonstrate that this small bonding ring component is negligible. The width of this mode is increased compared to the widths of the individual disk and ring plasmons, hence the DAR mode has a superradiant character. For the structural parameters discussed here, the width of the DAR mode is 0.38 eV, compared to a width of 0.32 eV of the disk dipole. We

point out that the antibonding combination of the disk and the antibonding dipolar ring mode is not visible in the extinction spectrum due to the strong damping at high energies.

Conversely, the mode below 1.5 eV, referred to as the DBR mode, results from a bonding combination of the disk dipole and the bonding-type ring dipole. The large energy difference between the DBR and antibonding ring mode and the charge distribution plot indicate the hybridized DBR mode has negligible admixture of the antibonding ring component. Because of the opposite alignment of disk and ring dipole for this combination, the net dipole moment of the hybridized mode is reduced, and it is of subradiant character. In this case, the radiative width is reduced to 0.16 eV, compared to that of 0.37 eV for the bonding ring dipole. This line narrowing, due to the decrease in radiative damping, should result in a high field enhancement and also a large sensitivity for changes in the refractive index of the environment.

To quantify the potential of a CRDC cavity for surface enhanced Raman scattering (SERS) at visible and near-infrared frequencies, surface enhanced infrared absorption spectroscopy (SEIRA) in the mid-IR, and LSPR sensing, we now quantify both the attainable field enhancement and frequency tunability of the DBR and DAR resonances for cavities on a silica substrate with $\varepsilon = 2.25$. While the hybridization of the individual ring and disk plasmons in the combined cavities and the changes in radiative width are most clearly illustrated in the plots of extinction versus energy/frequency as in Figure 1, we now switch to a description of the spectral position of the resonances in terms of wavelength, in order to aid the assessment of molecular sensing applications. We start with a quantification of the enhancement of the electric field for a cavity of the same dimensions as the CRDC presented in Figure 1. The extinction spectrum is shown in Figure 2a, and the electric field distribution of both the DAR and the DBR modes in various cut-planes in panels b and c, respectively. As expected, both modes show a slight redshift compared to the vacuum case, due to the fact that parts of the mode energies now reside in the higher permittivity substrate. Both the DAR and the DBR mode show large field enhancements in the 10 nm circular gap between the disk and the ring, due to the high spatial squeezing of the mode, akin to metal/insulator/metal waveguides.[29] We point out that the field enhancement is significantly higher than that of both individual disks and rings even for larger gap sizes than those presented here.[27]

The large field enhancements and spectral separation between the DAR and DBR modes suggests the potential usage of a CRDC as a multisensing platform, where both resonances overlap with excitation laser lines for SERS, and possibly also for SEIRA, if the DBR mode can be made to redshift further toward the mid-

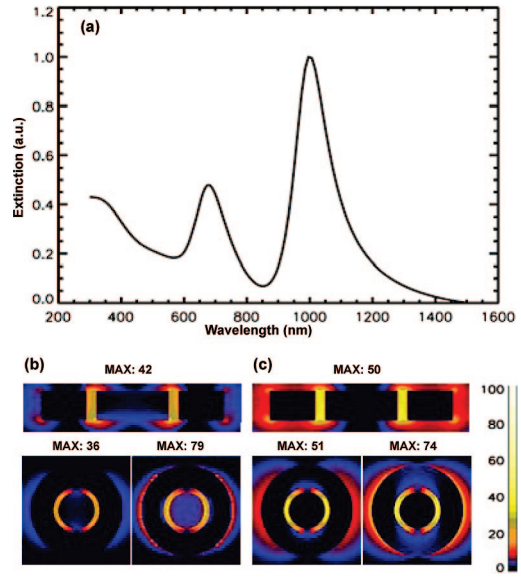

Figure 2. (a) Extinction spectrum of a Au CRDC of same dimensions as in Figure 1 but on a silica substrate ($\varepsilon = 2.25$). The DAR and DBR hybridized modes fall into the visible (679 nm) and near-infrared (1001 nm) part of the spectrum. (b) Electric field enhancement for the DAR mode in cut-planes through the symmetry axis of the system (top), and cross sections at medium height $H/2$ (lower left), and at the substrate interface (lower right). (c) Ditto for the DBR mode. The maximum field enhancement is indicated above each plot.

infrared for practically realizable structures. We now analyze this possibility in both Figures 3 and 4. The shifting of the two dipolar resonances with changes in the geometric parameters d_2, d_1, and D is most intuitively

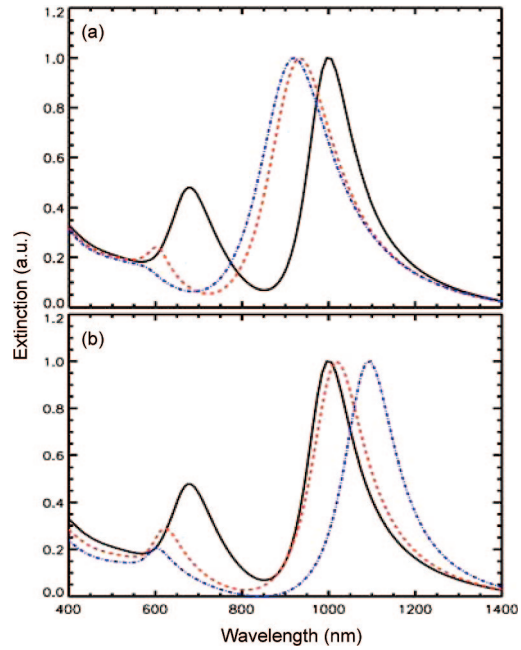

Figure 3. Structural tunability of DAR and DBR modes for a Au CRDC with $H = 50$ nm on silica. (a) Ring fixed with $d_1 = 100$ nm, $d_2 = 200$ nm, and varying disk diameter $D = 80$ nm (solid black), 60 nm (dashed red), and 40 nm (dash-dotted blue). (b) Disk and outer ring diameter fixed with $D = 80$ nm, $d_2 = 200$ nm, and varying inner ring diameter $d_1 = 100$ nm (black), 120 nm (dashed red), and 140 nm (dash-dotted blue).

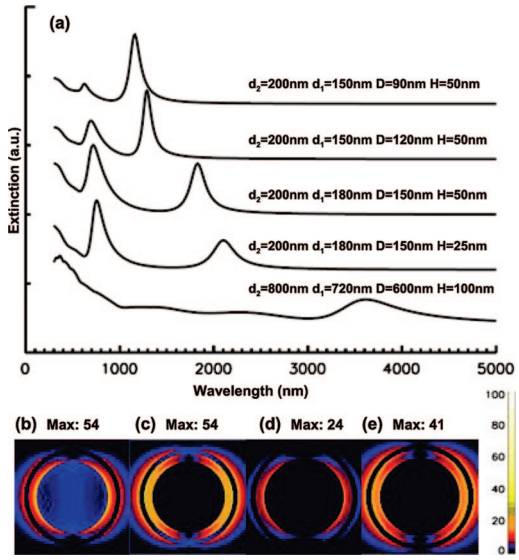

Figure 4. (a) Tunability of the CRDC through the near-infrared and toward the mid-infrared; panels b−e show the electric field enhancement at the substrate interface: (b) the DAR (λ = 755 nm) and (c) DBR (λ = 2101 nm) modes of the 4th system in panel a; (d) the DAR (λ = 2266 nm) and (e) the DBR (λ = 3620 nm) resonances for the 5th system in panel a. The maximum value of the field enhancement is shown on top of each plot.

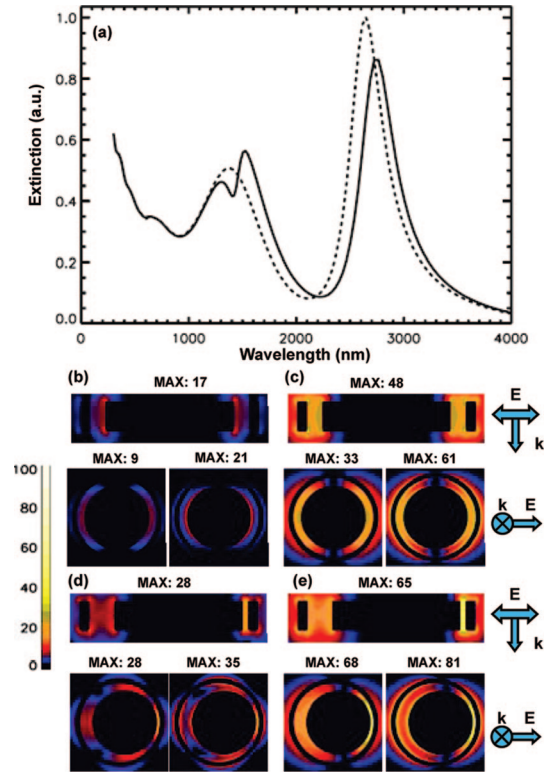

Figure 5. (a) Extinction cross section for a CRDC (dashed line) and NCRDC (solid line) Au cavity on a silica substrate (H = 75 nm, d_2 = 540 nm, d_1 =480 nm, D = 390 nm, offset of 30 nm between disk and ring center for NCRDC). For the CRDC, panels b and c show electric field enhancements for the DAR and DBR modes at 1372 and 2644 nm, respectively. For the NCRDC, panels d and e show electric field enhancements for the Fano resonance and the DBR mode at 1431 and 2748 nm, respectively. Each of these four panels show cut-planes through the symmetry axis of the system (top), the cross sections through the middle at H/2 (lower left), and at the substrate interface (lower right).

understood for the case of fixed ring geometry and varying disk diameter D, shown in Figure 3a for d_1 = 100 nm and d_2 = 200 nm. A widening of the gap due to a decrease in disk diameter from D = 80 nm (solid black curve) to 60 nm (dashed red curve) and finally 40 nm (dash-dotted blue curve) results in a blueshift of both DAR and DBR modes and a diminishing of their superradiant and subradiant characters, respectively, as expected owing to the decrease in interaction strengths and hence hybridization between the individual disk and ring plasmons. For fixed disk and outer ring diameter, but varying inner ring diameter, the strong dependence of the dipolar ring plasmons on ring width $d_2 - d_1$[7] has to be taken into account. The redshift of the bonding dipolar ring mode, and the blue shift of the antibonding dipolar ring mode, for increasing d_1 competes with the spectral shifts induced by the diminishing hybridization between disk and ring modes. For a structure with D = 80 nm and d_2 = 200 nm, the net result for an increase of d_1 from 100 nm (black curve) to 120 nm (dashed red curve) and 140 nm (dash-dotted blue curve) results in a redshift of the DBR and a blueshift of the DAR mode, as shown in Figure 3b. Increasing the parameter space for variations in d_1 and D while keeping the outer diameter fixed to d_2 = 200 nm, it can be shown that the whole spectral region between 600 and 1200 nm, relevant for SERS, is accessible for the DAR and DBR resonances. It is illuminating to note that for rings of smaller widths, the DBR mode shows significant shifts further out toward the mid-infrared, while the DAR mode, mainly composed of the dipolar disk resonance for larger gaps, stays within the visible frequency window, as shown in the extinction spectra of Figure 4a for a number of examples. An increase the total size of the structure (Figure 4a, bottom curve) further allows for the DBR resonance to move to mid-infrared frequencies due to retardation effects, making therefore also the local enhancement of radiation in this spectral window possible, for applications in SEIRA. The broad DAR resonance spanning parts of the visible and near-IR regime and the sharp DBR resonance in the mid-IR of the ring/disk cavity make this structure a strong candidate as a common substrate for SERS and SEIRA. Figure 4 panels b−e are showing the electric field enhancement on the interface surface between the CRDC and the dielectric substrate for the bottom two structures in Figure 4a.

The enhancement of the electric field can be further increased by breaking the symmetry of the system, which we will now analyze for a NCRDC with a displacement of the disk center by δ in relation to the center of the ring. A first example is shown in Figure 5, which similar to Figure 2 shows both extinction spectra and the distribution of the electric field in various

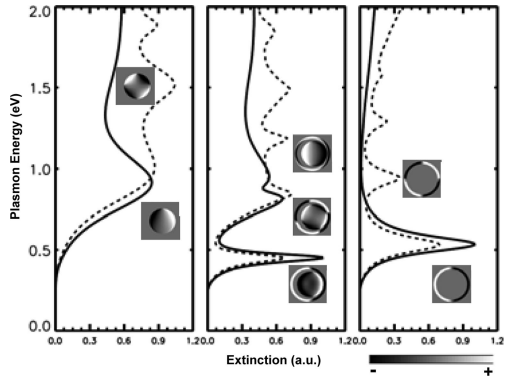

Figure 6. Hybridization diagram for the NCRDC in Figure 5. The solid lines correspond to extinction cross sections obtained for normal incidence, and the dashed lines for those obtained using illumination under grazing incidence angle. For the individual disk (left) and ring (right), charge distributions at the resonance frequencies of the dipolar and quadrupolar mode are plotted under grazing incidence illumination. The center panel shows the extinction spectra of the combined structures, and the charge distributions show the DAR, DBR, and bonding quadrupolar mode obtained under normal incidence illumination.

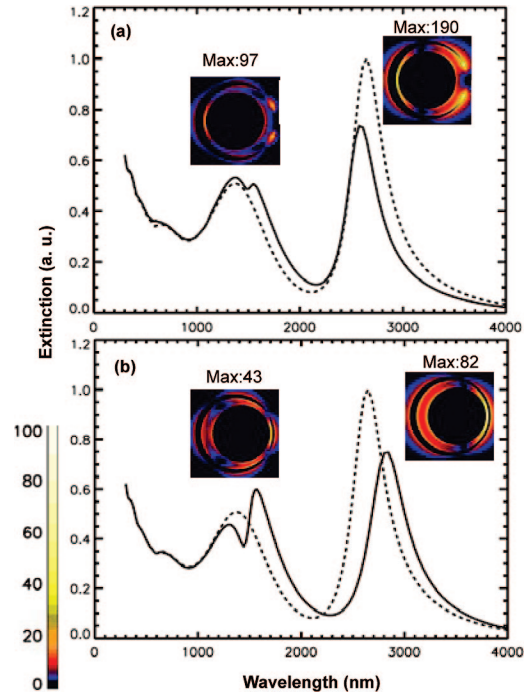

Figure 7. Structural tunability of the Fano resonance. The dashed lines show extinction spectra for a CRDC on silica with $d_2 = 540$ nm, $d_1 = 480$ nm, $D = 390$ nm, and $H = 75$ nm. The solid lines show extinction spectra for the NCRDC, with the associated field distributions at the Fano and DBR resonances at the substrate interface. In panel a, the center of the circle outlining the inner surface of the ring is offset by 30 nm compared to that of the outer surface. In panel b, this offset is 15 nm, and additionally the center of the disk is offset by 45 nm.

cut-planes, for a Au NCRDC on silica with $d_2 = 540$ nm, $d_1 = 480$ nm, $D = 390$ nm, $H = 75$ nm, and $\delta = 30$ nm. The concentric system exhibits the subradiant DBR mode at a wavelength of 2644 nm and the superradiant DAR mode at 1372 nm, respectively, as shown in the extinction spectrum (Figure 5a, dotted curve). The associated field distributions and maximum field enhancements for both modes are shown in panels b and c, with maximum field enhancements of 21 for the DAR and 61 for the DBR, respectively. For the symmetry-broken system (solid curve in panel a), both modes show a slight redshift, and additionally a Fano-type asymmetric interference profile appears within the broad DAR mode, due to the overlap with a narrow quadrupolar ring resonance (QR), as will be discussed further. As can be intuitively expected, the maximum enhancement of the electric field increases with respect to the concentric system, at the position of decreased gap size, as shown in panels d and e for the Fano resonance (35) and the DBR mode (81).

We now shift our focus to an analysis of the Fano-type interference phenomenon, in terms of its spectral tunability, attainable field enhancement, and refractive index sensitivity. As mentioned above, it results from the overlap of the broad DAR mode with a narrow QR mode,[28] which is clearly shown using a hybridization diagram akin to Figure 1b, but now for a symmetry-broken NCRDC. This is presented in Figure 6, for a cavity with the same geometric parameters as that of Figure 5. To reveal the QR mode for the individual ring cavity, the extinction spectra are shown both for illumination under normal incidence (solid curves), and under grazing incidence (dotted curves), which reveal higher-order modes of symmetric structures due to retardation effects.[20] The symmetries of the modes are clearly revealed in the insets showing the associated surface charge distributions. For the NCRDC (middle panel), the overlap of the broad DAR mode with the sharper QR mode of the ring around 0.9 eV satisfies the conditions for EIT, which leads to the appearance of the QR as a narrow asymmetric Fano line shape in the broad continuum of the DAR. This phenomenon generally occurs in classical oscillator systems with a dispersive coupling of a bright, broad continuum-like mode and a sharper, dark mode.[26] Our interpretation is backed up by the charge distributions obtained at the respective features of DBR, DAR, and bonding QR resonances.

Apart from creating an offset δ between the respective centers of the disk and the ring, symmetry-breaking can also be achieved *via* an asymmetry in the width of the ring, achieved *via* an offset between the centers of the circles outlining the inner and outer ring surfaces. Representative examples are shown in Figure 7, which show extinction spectra both for a CRDC with the same geometric parameters as that described in Figure 5 (dotted curves), and for two distinct NCRDCs. In panel a, the centers of the rings outlining the inner and outer ring surfaces show an offset of 30 nm, while in panel b this offset is 15 nm, with an additional disk offset $\delta = 45$ nm. The insets show the respective electric field distributions both at the position of the Fano resonance and

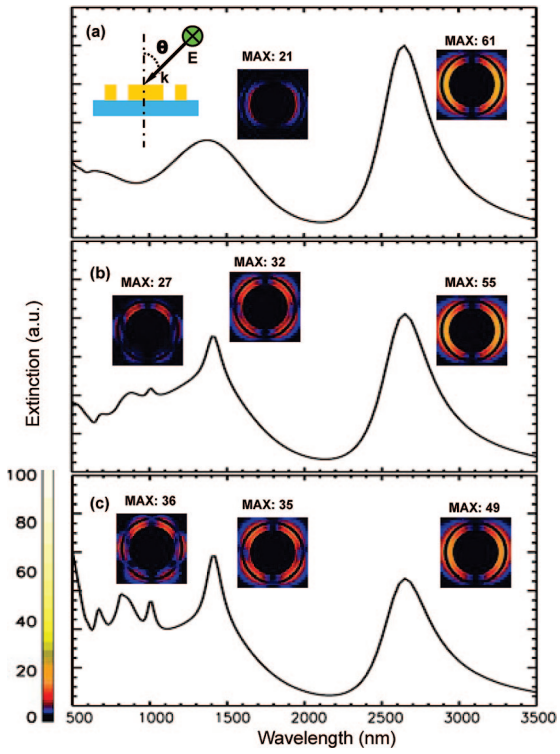

Figure 8. Extinction spectra of a CRDC on a silica substrate for different incident angles θ = 0° (a), 45° (b), and 90° (c) as defined in the inset. The geometric parameters of the system are d_2 = 540 nm, d_1 = 480 nm, D = 390 nm, and H = 75 nm. The local electric field enhancement along the substrate interface are plotted at the resonance frequencies. For panel a, field enhancements are shown for the DBR (2645 nm) and DAR (1372 nm). For panels b and c, the field enhancements are for dipolar (2645 nm), quadrupolar (1411 nm), and octupolar (1008 nm) resonances. Maximum values are shown on top of each plot.

the DBR. Using various combinations of these two geometric variations to break symmetry, it is clear that the spectral position of the Fano resonance can be tuned throughout the near-infrared spectral region, with associated substantial field enhancements (shown in the insets).

The higher order modes responsible for the Fano-type interference phenomena in symmetry-broken structures are of course also relevant for a CRDC illuminated at an angle. In this case, higher-order modes are directly excited due to retardation effects, akin to those previously described for single rings.[20] Because of the finite speed of light, when a wave hits the structure from the side, only part of it is polarized, and the instantaneous polarization of surface charges can be expanded as a superposition of multipolar resonances. This leads to the excitation of the multipolar plasmon resonances of a disk/ring cavity without breaking the geometrical symmetry. We mention this fact as these higher order modes also show a significant field enhancement, as shown in Figure 8 for the CRDC described previously in Figure 5. In the inset of panel a, we define the incident angle θ as the angle between incident direction and the axis of the CRDC. The polarization is always perpendicular to the axis of the structure. For normal incident angle θ = 0°, just as shown before, two characteristic resonances, a low energy sharp DBR mode and a high energy broad DAR mode appears in the spectrum. As θ increased to 45° (b), sharper features appear within the broad DAR resonance. The insets depicting electric field enhancement contour plots reveal these features as bonding multipolar resonances of the ring-disk cavity, with maximum field enhancements on the order of 30 for this specific set of geometrical parameters. As θ increases to 90° (c), that is, grazing incidence, several modes of higher multipolar orders are clearly visible in the extinction spectrum. It is interesting to note that the maximum enhancement of the electric field increases with increasing illumination angle for the multipolar modes, but decreases for the DBR, due to its dipolar nature. This can be intuitively understood by decomposing the excitation pulse charge distribution into a set of multipolar orders, noting that the overlap with a dipolar charge distribution decreases as the illumination direction moves from normal to grazing incidence. The large electric field enhancements for the multipolar bonding modes at visible frequencies and the DBR resonance in the mid-IR suggest that the concentric ring-disk cavity can be utilized as a common substrate for SERS and SEIRA particularly well with angular incidence illumination, that is, highly focused beams.

We now turn to a more quantitative description of the Fano interference phenomenon using an analytic model for the absolute value of the polarizabilities of our cavity structures. Recent studies have shown that the amplitude of transmission or reflection of a plasmonic lattice can be well described by a Fano-type line shape.[23,30] In the following, we demonstrate that the absolute value of the polarizabilities $|\alpha|$ of disk, ring, and CRDC can also be expressed using a Fano interference model. To this end, we first obtain the normalized charge distribution $\rho(\vec{x}, \omega)$ by evaluating the divergence of the normalized electric field $\vec{E}(\vec{x}, \omega)/E_0(\omega)$, which is acquired from a Fourier transformation of $E(\vec{x}, t)$ in our FDTD simulations. Then the polarizability $\vec{\alpha}$ is calculated *via* a volume integration $\vec{\alpha}(\omega) = \int \vec{x}\ \rho(\vec{x}, \omega)\, d^3x$. Figure 9 shows plots for $|\alpha|$ as a function of energy. The black curves in panels (a−c) are the FDTD calculated polarizabilities $|\alpha|$ for a disk, a ring, and a CRDC, respectively, with geometrical parameters H = 50 nm, D = 130 nm, d_2 = 200 nm, and d_1 = 150 nm. The DAR and DBR modes are clearly visible.

The calculated polarizabilities may now be fitted with an analytical Fano interference model:

$$|\alpha|(\omega) = a_r - \sum_j \frac{b_j \Gamma_j e^{i\varphi_j}}{\omega - \omega_j + i\Gamma_j} \qquad (1)$$

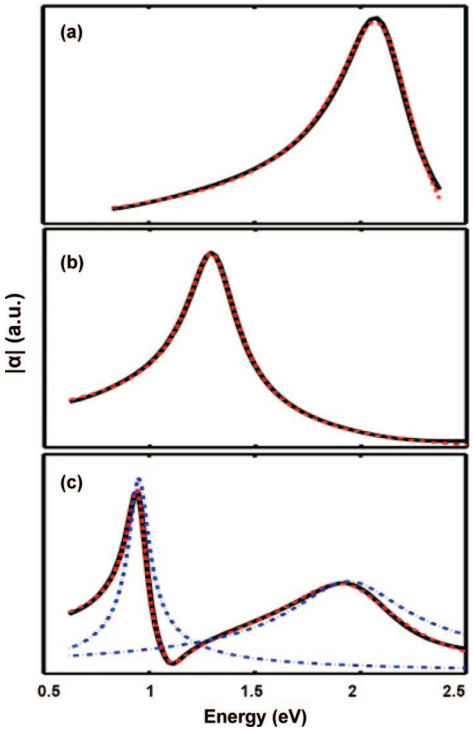

Figure 9. Polarizability of disk, ring, and their combinations. Black solid lines are calculated from FDTD, and red dashed lines are the analytical Fano interference model described in the main text: (a) polarizability for gold disk in vacuum with $D = 130$ nm, $H = 50$ nm. The parameters are: $a_r = 0.0011$, $b_1 = 0.0050$, $\Gamma_1 = 0.1784$ eV, $\omega_1 = 2.1072$ eV. (b) Polarizability of a gold ring with $d_2 = 200$ nm, $d_1 = 150$ nm, $H = 50$ nm. The fitting parameters are $a_r = 0.0021$, $b_1 = 0.0247$, $\Gamma_1 = 0.1139$ eV, $\omega_1 = 1.2992$ eV. (c) Polarizability for the concentric combination of above two. Dot−dashed blue lines are the plot of individual poles. The parameters are $a_r = 0.0023$, $b_1 = 0.0093$, $\Gamma_1 = 0.2575$ eV, $\omega_1 = 1.9432$ eV, $\phi_1 = 0°$, $b_2 = 0.0198$, $\Gamma_2 = 0.0425$ eV, $\omega_2 = 0.951$ eV, $\phi_2 = 36.5°$.

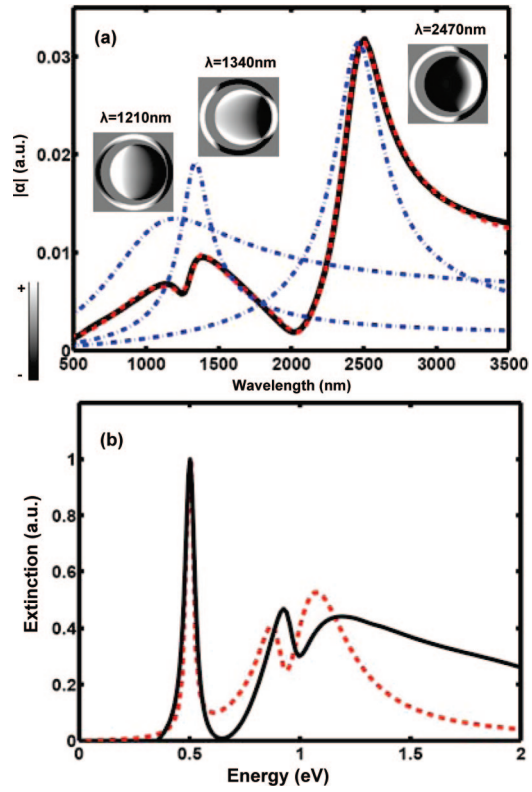

Figure 10. (a) Fitting of the absolute value of the polarizability of a NCRDC in vacuum ($d_2 = 540$ nm, $d_1 = 480$ nm, $D = 390$ nm, $H = 75$ nm, and $\delta = 30$ nm): FDTD (black) and 3-pole Fano model (red dashed). The parameters are $a_r = -0.0026$, $b_1 = 0.0192$, $\Gamma_1 = 0.061$ eV, $\omega_1 = 0.9259$ eV, $\phi_1 = 0°$, $b_2 = 0.0135$, $\Gamma_2 = 0.4124$ eV, $\omega_2 = 1.0306$ eV, $\phi_2 = 211°$, $b_3 = 0.0316$, $\Gamma_3 = 0.0289$ eV, $\omega_3 = 0.5038$ eV, $\phi_3 = 263°$. Blue dot−dashed lines are the individual modes. Insets are the charge distribution of each mode: DAR ($\lambda = 1210$ nm), quadrupole ($\lambda = 1340$ nm), DBR ($\lambda = 2470$ nm). (b) Fitting of the FDTD extinction spectrum (black) using the Alzar model (red dashed) using the same mode energies ω_i, and damping factors Γ_i. The coupling coefficient between the superradiant mode and quadrupolar is 0.15, and the force applied on the superradiant and subradiant mode is 2.5 and 1.0.

where a_r is the constant amplitude of the background, b_j and ϕ_j specify the amplitudes and the phases of each plasmon eigenmode, and ω_j and Γ_j represent their resonance energies and linewidths. For the individual disk and the ring shown in Figure 9a,b, the polarizabilities $|\alpha|$ can be described by a single plasmon mode, neglecting the low-intensity antibonding ring mode. The fits are almost indistinguishable from the FDTD results. For the CRDC shown in Figure 9c, two modes representing the DBR and DAR have to be used in eq 1 and are shown with the blue-dash−dotted lines. Also in this case, a very good agreement with the FDTD results is obtained. The line width of the DBR mode of 0.0425 eV is significantly reduced from that of the ring (0.1139 eV), characteristic of its subradiant nature. Conversely the DAR mode shows an increased line width of 0.2575 eV.

For the NCRDC, symmetry breaking enables direct excitation of the QR mode. To account for this, an additional mode is included in the interference model eq 1. Figure 10a compares the FDTD polarizability with a 3-pole Fano model eq (1) with parameters described in the caption. As for the concentric system in Figure 9, an excellent fit is obtained. The contributions from the individual resonances are shown by the blue dash-dotted lines. The microscopic nature of the three relevant modes is further corroborated *via* their surface charge distributions as plotted in the inset. The overlap of the spectrally sharper QR with the continuum of the DAR mode is clearly visible.

The plasmonic Fano interference phenomenon can also be modeled using a spring-mass model developed by Alzar and co-workers.[26] A fit to the FDTD extinction spectrum is shown in Figure 10b (dashed red curve), using the same plasmon mode energies ω_i and damping factors Γ_i as used for the polarizability fit in Figure 10a. The excellent agreement with the FDTD results obtained using this mechanical model is noteworthy.

We finish this discussion with a glimpse of the wide amount of spectral tunability of the Fano interference feature as the coupling conditions between the three resonance channels DAR, DBR, and QR, are varied, achieved *via* changes in the respective geometrical pa-

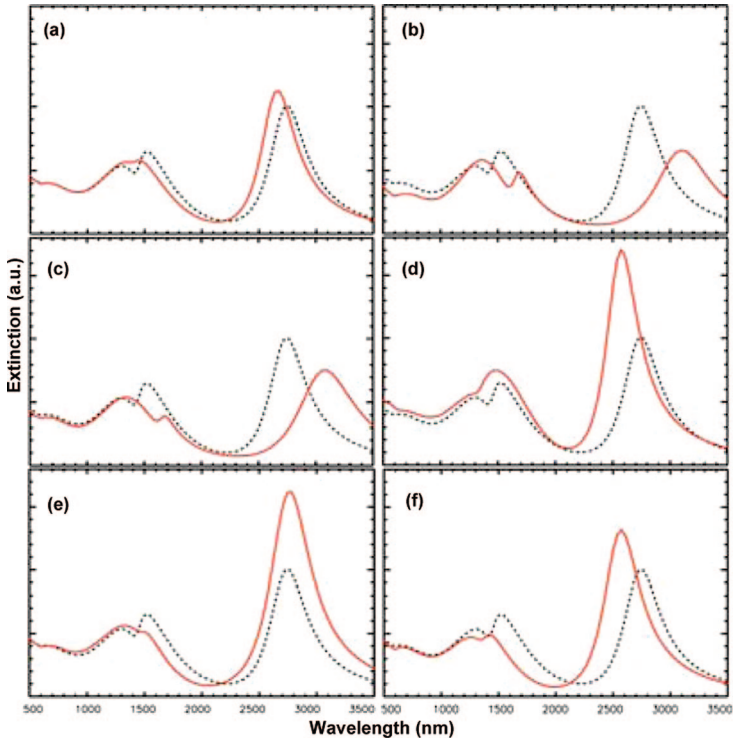

Figure 11. Structural tunability of Fano resonances. The dotted lines are the extinction spectrum of a NCRDC on silica with d_2 = 540 nm, d_1 = 480 nm, D = 390 nm, H = 75 nm, and δ = 30 nm. The red lines are the extinction spectra resulting from a change of the structural parameters: (a) δ = 15 nm, (b) H = 36 nm, (c) d_1 = 510 nm, (d) d_2 = 600 nm, (e) d_1 = 540 nm and d_2 = 600 nm, and (f) D = 360 nm.

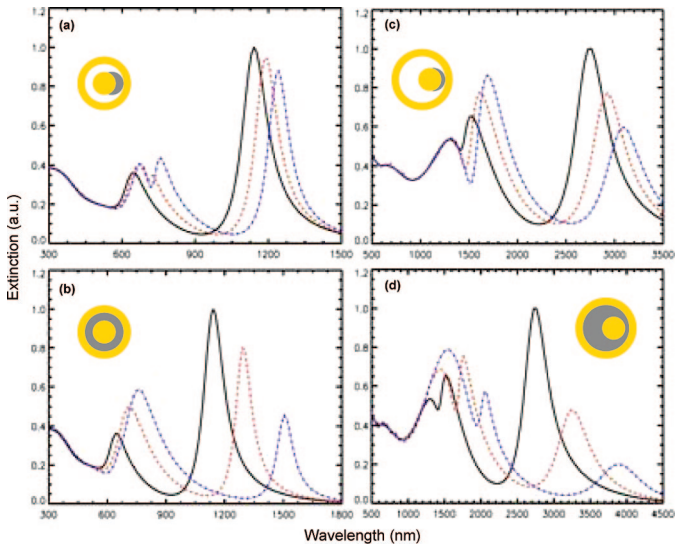

Figure 12. Refractive index sensitivity for concentric and nonconcentric ring/disk cavity. Panels a and b are for a CRDC on silica substrate with d_2 = 200 nm, d_1 = 140 nm, D = 100 nm, H = 50 nm. Panels c and d are for a NCRDC on silica substrate with d_2 = 540 nm, d_1 = 480 nm, D = 390 nm, H = 75 nm, δ = 30 nm: (a, c) partial dielectric filling of the cavity; (b, d) complete filling. As shown in the schematics in each subplot, yellow represents gold, gray is for dielectrics, and white is for vacuum. The dielectric permittivities are ε = 1 (black), ε = 2.25 (red dotted), and ε = 4 (blue dash−dotted).

rameters of the disk and ring forming a NCRDC. Figure 11 shows a number of representative examples outlining how changes in δ, H, d_1, d_2, and finally D affect the extinction spectra.

Lastly, we examine the sensitivity of the plasmon resonance spectrum of both the CRDC and NCRDC to changes in the refractive index in the gap region between disk and ring, where small molecules are expected to concentrate because of strong gradient forces induced by plasmons. As the hybridization between the individual disk and ring modes, and the Fano interference phenomenon, are likely to be strongly affected by molecular screening, a high LSPR sensitivity of the respective spectral features, expressed either in nm/RIU or the figure of merit (FOM) introduced by van Duyne and co-workers,[31] can be expected. As shown in Figure 12, significant redshifts of the DBR, DAR, and Fano-feature occur for CRDCs and NCRDCs, respectively, if either the whole gap region or only a part is filled with a dielectric medium. The LSPR shifts of the DBR mode for CRDC are respectively 97 nm/RIU and 357 nm/RIU for a partial and complete dielectric filling cavity. The corresponding FOMs are 0.73 and 2.2 for partial and complete filling. For the DBR mode of the NCRDC the LSPR shifts are 331 nm/RIU for partial filling and 1116 nm/RIU for complete dielectric filling of the cavity. The the fwhm for the DBR in the NCRDC is 0.0669 eV, giving FOMs of 0.72 for a partially filled cavity and 1.9 for a completely filled cavity. As defined in previous work,[28] the fwhm for the Fano resonance in the NCRDC is 0.072 eV. The corresponding LSPR shift and FOM are 129 nm/RIU and 0.95 for partially filled cavity, and 534 nm/RIU and 3.2 for a completely filled cavity. Even larger LSPR shifts and FOMs can be obtained for a better optimized NCRDC.[28] It is noteworthy to point out that only partially filling the gap of the CRDC (Figure 12a) also leads to the appearance of a Fano-interference feature due to the associated break in symmetry. Rather than a mere shift of the extinction DAR extinction peak, this drastic change in line shape might be very amendable for LSPR sensing purposes.

All the above studies are conducted in air environment. We also examine the situation when the structure is submersed in water which is how some LSPR applications are performed. In an aquous environment, the spectra are slightly red-shifted and the LSPR shifts are reduced slightly. No qualitatively changes are found when the surrounding medium is varied from air to water. Lastly we point out that spectral shifts of similar magnitudes were found for refractive index changes occurring in a nanometric layer covering the whole structure, rather than the spatially smaller gap region. For the CRDC, as expected such homogeneous coverage

did not induce a Fano resonance, as no symmetry breaking occurs.

CONCLUSIONS

Concentric and nonconcentric plasmonic ring/disk nanocavities constitute a rewarding physical implementation of classical oscillator systems exhibiting subradiant and superradiant plasmon resonances. In systems with broken symmetry, additional Fano-type interference phenomena appear due to interactions of higher order modes with the broad dipolar continuum. The high amount of field localization and associated enhancement in the nanogap region inside the cavity result in an exceptionally high sensitivity of the resonant features with local refractive index, which together with the large amount of spectral tunability from the visible to the mid-infrared makes these cavities a promising platform for surface enhanced molecular sensing.

METHODS

All spectra presented in this publication are calculated using the finite-difference time-domain (FDTD) method.[32,33] The dielectric response of Au is modeled using a 4 Lorentzian term fit to the experimentally measured permittivity,[34,35] and the individual cavity structures are illuminated with a plane-wave pulse. Extinction spectra are then obtained *via* integration of the power flow over the computational boundaries and an appropriate near- to far-field transform.[33]

Acknowledgment. Y.S. and S.M. acknowledge support from UK Engineering and Physical Sciences Research Council (EPSRC). F.H. and P.N. acknowledge support from the U.S. Army Research Laboratory and the U.S. Army Research Office under contract/grant number W911NF-04-1-0203, the Robert A. Welch Foundation under grant C-1222, and by the National Science Foundation under grant number CNS-0421109. P.V.D. acknowledges financial support from the FWO (Flanders).

REFERENCES AND NOTES

1. Maier, S. A. *Plasmonics—Fundamentals and Applications*, 1st ed.; Springer: New York, 2007.
2. Lal, S.; Link, S.; Halas, N. J. Nano-Optics from Sensing to Waveguiding. *Nat. Photon.* **2007**, *1*, 641–648.
3. Atwater, H. A. The Promise of Plasmonics. *Sci. Am.* **2007**, *296*, 56–63.
4. Maier, S. A.; Atwater, H. A. Plasmonics: Localization and Guiding of Electromagnetic Energy in Metal/Dielectric Structures. *J. Appl. Phys.* **2005**, *98*, 011101.
5. Mock, J. J.; Barbic, M.; Smith, D. R.; Schultz, D. A.; Schultz, S. Shape Effects in Plasmon Resonance of Individual Colloidal Silver Nanoparticles. *J. Chem. Phys.* **2002**, *116*, 6755–6759.
6. Kuwata, H.; Tamaru, H.; Esumi, K.; Miyano, K. Resonant Light Scattering from Metal Nanoparticles: Practical Analysis beyond Rayleigh Approximation. *Appl. Phys. Lett.* **2003**, *83*, 4625–2627.
7. Aizpurua, J.; Hanarp, P.; Sutherland, D. S.; Käll, M.; Bryant, G. W.; de Abajo, F. J. G. Optical Properties of Gold Nanorings. *Phys. Rev. Lett.* **2003**, *90*, 057401.
8. Maier, S. A. Plasmonic Field Enhancement and SERS in the Effective Mode Volume Picture. *Opt. Express* **2006**, *14*, 1957–1964.
9. Miyazaki, H. T.; Kurokawa, Y. Squeezing Visible Light Waves into a 3-nm-Thick and 55-nm-Long Plasmon Cavity. *Phys. Rev. Lett.* **2006**, *96*, 097401.
10. Kneipp, K.; Kneipp, H.; Itzkan, I.; Dasari, R. R.; Feld, M. S. Surface Enhanced Raman Scattering and Biophysics. *J. Phys. Cond. Mater.* **2002**, *14*, R597−R624.
11. Xu, H.; Aizpurua, J.; Kaell, M.; Apell, P. Electromagnetic Contributions to Single-Molecule Sensitivity in Surface-Enhanced Raman Scattering. *Phys. Rev. E* **2000**, *62*, 4318–4324.
12. Anker, J. N.; Hall, W. P.; Lyandres, O.; Shah, N. C.; Zhao, J.; Duyne, R. P. V. Biosensing with Plasmonic Nanosensors. *Nat. Mater.* **2008**, *7*, 442–453.
13. Lal, S.; Clare, S.; Halas, N. J. Nanoshell-Enabled Photothermal Cancer-Therapy: Impending Clinical Impact. *Acc. Chem. Res.* **2008**, *41*, 1842–1851.
14. Wang, H.; Wu, Y.; Lassiter, B.; Nehl, C. L.; Hafner, J. H.; Nordlander, P.; Halas, N. J. Symmetry Breaking in Individual Plasmonic Nanoparticles. *Proc. Natl. Acad. Sci. U.S.A.* **2006**, *103*, 10856–10860.
15. Fedotov, V. A.; Rose, M.; Prosvirnin, S. L.; Papasimakis, N.; Zheludev, N. I. Sharp Trapped-Mode Resonances in Planar Metamaterials with a Broken Structural Symmetry. *Phys. Rev. Lett.* **2007**, *99*, 147401.
16. Liu, N.; Guo, H.; Kaiser, S.; Schweizer, H.; Giessen, H. Plasmon Hybridization in Stacked Cut-Wire Metamaterials. *Adv. Mater.* **2007**, *19*, 3628.
17. Liu, N. A.; Fu, L.; Kaiser, S.; Schweizer, H.; Giessen, H. Plasmonic Building Blocks for Magnetic Molecules in Three-Dimensional Optical Metamaterials. *Adv. Mater.* **2008**, *20*, 3859–3865.
18. Christ, A.; Martin, O. J. F.; Ekinei, Y.; Gippius, N. A.; Tikhodeev, S. G. Symmetry Breaking in a Plasmonic Metamaterial at Optical Wavelength. *Nano Lett.* **2008**, *8*, 2171–2175.
19. Kottmann, J. P.; Martin, O. J. F. Retardation-Induced Plasmon Resonances in Coupled Nanoparticles. *Opt. Lett.* **2001**, *26*, 1096.
20. Hao, F.; Larsson, E. M.; Ali, T. A.; Sutherland, D. S.; Nordlander, P. Shedding Light on Dark Plasmons in Gold Nanorings. *Chem. Phys. Lett.* **2008**, *458*, 262–266.
21. Prodan, E.; Radloff, C.; Halas, N. J.; Nordlander, P. A Hybridization Model for the Plasmon Response of Complex Nanostructures. *Science* **2003**, *203*, 419–422.
22. Le, F.; Brandl, D. W.; Urzhumov, Y. A.; Wang, H.; Kundu, J.; Halas, N. J.; Aizpurua, J.; Nordlander, P. Metallic Nanoparticle Arrays: A Common Substrate for both Surface-Enhanced Raman Scattering and Surface-Enhanced Infrared Absorption. *ACS Nano* **2008**, *2*, 707–718.
23. Christ, A.; Ekinei, Y.; Solak, H. H.; Gippius, N. A.; Tikhodeev, S. G.; Martin, O. F. J. Controlling the Fano Interference in a Plasmonic Lattice. *Phys. Rev. B* **2007**, *76*, 201405R.
24. Bachelier, G.; Russier-Antoine, I.; Benichou, E.; Jonin, C.; del Fatti, N.; Valee, F.; Brevet, P.-F. Fano Profiles induced by Near-Field Coupling in Heterogeneous Dimers of Gold and Silver Nanoparticles. *Phys. Rev. Lett.* **2008**, *101*, 107401.
25. Zhang, S.; Genov, D. A.; Wang, Y.; Liu, M.; Zhang, X. Plasmon-Induced Transparency in Metamaterials. *Phys. Rev. Lett.* **2008**, *101*, 047401.
26. Alzar, C. L.G.; Martinez, M. A. G.; Nussenzveig, P. Classical Analog of Electromangetically Induced Transparency. *Am. J. Phys.* **2002**, *70*, 37–41.
27. Hao, F.; Nordlander, P.; Burnett, M. T.; Maier, S. A. Enhanced Tunability and Linewidth Sharpening of Plasmon Resonances in Hybridized Metallic Ring/Disk Nanocavities. *Phys. Rev. B* **2007**, *76*, 245417.
28. Hao, F.; Sonnefraud, Y.; Dorpe, P. V.; Maier, S. A.; Halas, N. J.; Nordlander, P. Symmetry Breaking in Plasmonic Nanocavities: Subradiant LSPR Sensing and a Tunable Fano Resonance. *Nano Lett.* **2008**, *8*, 3983–3988.

29. Veronis, G.; Fan, S. Guided Subwavelength Plasmonic Mode supported by a Slot in a Thin Metal Film. *Opt. Lett.* **2005**, *30*, 3359–3361.
30. Ropers, C.; Park, D. J.; Stibenz, G.; Steinmeyer, G.; Kim, J.; Kim, D. S.; Lienau, C. Femtosecond Light Transmission and Subradiant Damping in Plasmonic Crystals. *Phys. Rev. Lett.* **2005**, *94*, 113901.
31. Sherry, L. J.; Chang, S. H.; Schatz, G. C.; van Duyne, R. P.; Wiley, B. J.; Xia, Y. Localized Surface Plasmon Resonance Spectroscopy of Single Silver Nanocubes. *Nano Lett.* **2005**, *5*, 2034–2038.
32. Oubre, C.; Nordlander, P. Optical Properties of Metallodielectric Nanostructures Calculated Using the Finite Difference Time Domain Method. *J. Phys. Chem. B* **2004**, *108*, 17740–17747.
33. Taflove, A.; Hagness, S. C. *Computational Electrodynamics: The Finite-Difference Time Domain Method*; Artech House, INC.: Norwood, MA, 2005.
34. Hao, F.; Nordlander, P. Efficient Dielectric Function for FDTD Simulation of the Optical Properties of Gold and Silver Nanostructures. *Chem. Phys. Lett.* **2007**, *446*, 115–118.
35. Johnson, P. B.; Christy, R. W. Optical Constants of the Noble Metals. *Phys. Rev. B* **1972**, *6*, 4370–4379.